Journal of Materials Chemistry A

ARTICLE

Supporting Information

Block Copolymer Templated Synthesis of PtIr Bimetallic Nanocatalysts for the Formic Acid Oxidation Reaction

Audrey K. Taylor,[a] Diane S. Perez,[a] Xin Zhang,[c] Brandy K. Pilapil,[c] Mark H. Engelhard,[d] Byron D. Gates,[c] and David A. Rider[a,b]

[a] Department of Chemistry, Western Washington University, 516 High St., Bellingham WA 98225, USA
[b] Department of Engineering and Design, Western Washington University, 516 High St., Bellingham WA 98225, USA
[c] Department of Chemistry and 4D LABS, Simon Fraser University, 8888 University Drive, Burnaby BC V5A 1S6, Canada
[d] Environmental Molecular Sciences Laboratory, Pacific Northwest National Laboratory, Richland, Washington 99352, United States

*Corresponding Author: David A. Rider
Email address: david.rider@wwu.edu

The FEI Tecnai Osiris TEM instrument was used for transmission electron microscopy and energy dispersive X-ray mapping. Magnification calibration was performed using an automated procedure with a standardized Au-Pd grating. To ensure accuracy in the determination of lattice parameters by selected area electron diffraction, samples were studied with the same imaging conditions as those for an Al calibration standard. Typically, the data images and/or diffraction patterns of experimental samples are obtained followed by the study of the polycrystalline Al standard under the same electrical and magnetic conditions (i.e. the same lens current, high voltage, and magnification/camera length) to confirm the calibration accuracy. From a typical SAED image, the lattice parameters are assigned as per the below d-spacings for Al.

Miller Indices (hkl)	**Lattice Spacing (Å)**	**Normalized Intensity**	**Lattice Constant (Å)**
111	2.338	100	4.05
200	2.024	47	4.048
220	1.431	22	4.047
311	1.221	24	4.0489
222	1.169	7	4.0495
400	1.0124	2	4.0496
331	0.9289	8	4.049

Following the assignment of the d-spacings, a calibration constant (K) is calculated using the formula $K = S \times d$. K encompasses the wavelength of the electron beam, camera length and the associated variation in the crystallographic data, S represents the diameter of a diffraction ring in centimeters and d is the interplanar spacing in angstroms. The tolerance level for variation in the values for calibration constant for the first five lines is 1%. The imaging software is integrated with this calibration data to standardize the reciprocal readings of lattice spacing information acquired from FFT interpretations.

Table S1: Brief comparison of catalytic activity for formic acid oxidation reported for several binary and ternary systems.

Binary System	Catalytic Activity
PdPt[S1]	A mass activity of 1200 A/g was produced for the I_1 peak for a nanoporous alloy with a composition of $Pd_{80}Pt_{20}$.
PdCu[S2]	The I_1 peak was used for comparison and a current density value of ~ 0.45 mA/cm^2 was reported for a layered thin films of PdCu.
PtRu[S3]	The catalytic activity of Pt_7Ru_3 nanowires were evaluated for formic acid oxidation. A current density of ~1.5 mA/cm^2 was reported.
PtRuFe[S3]	The I_1 peak demonstrated a current density of ~2.1 mA/cm^2 for a reported composition of $Pt_7Ru_{1.5}Fe_{1.5}$.
PtFe[S3]	A current density of ~0.55 mA/cm^2 was reported for the I_1 peak produced from Pt_7Fe_3 nanowires.
PdNi[S4]	A composition of $Pd_{81}Ni_{19}$ showed a current density of ~1.75 mA/cm^2 for the I_1 peak.
PdNiCu[S4]	A trimetallic catalyst of $Pd_{57}Ni_{13}Cu_{30}$ exhibited a current density of 3.3 mA/cm^2 for the I_1 peak.
FePt[S5]	The I_1 peak was used for comparison and a current density of 104 mA/cm^2 was produced from the best preforming catalyst, $Fe_{42}Pt_{58}$.
PdPt[S6]	Formic acid oxidation was assessed using cyclic voltammetry and chronoamperometry. The I_1 peak was used for comparison and a mass activity value of 0.0023 A/g was reported for $Pd_{100}Pt_0$/CNT.
PtAu[S7]	Formic acid electrooxidation was characterized by mass activity values and 8000 A/g was reported for the I_3 peak of a NPG-Pt_1Au_2 catalyst.
PtPb[S8]	A mass activity value of 1330 A/g for the I_1 peak of Pd-Pt catalyst was compared and reported to monometallic Pd and Pt for formic acid oxidation. The current density was normalized to catalyst loading and particle size was also used to characterize activity.
FePt[S9]	Formic acid oxidation was catalyzed by Fe_xPt_{100-x} catalysts and a current density of 0.5 mA/cm^2 was reported for the I_1 peak. Voltammetric currents were normalized to the Pt active surface area. The best preforming catalyst was considered to be the $Fe_{20}Pt_{80}$ catalyst.
PtRu[S10]	Nanocrystals of Pt-Ru were studied catalytically by formic acid oxidation. A current density of ~5 mA/cm^2 and a mass activity of ~140 A/g were reported and compared to that of a commercial Pt-Ru standard.

Table S2. SFM-estimated height, FWHM, and periodicity for each PS-*b*-P4VP template cast onto ITO substrates. Dimensions are estimated from the mean of 5 sets of 3 aligned micelles in the SFM images.

Dimension	PS_n-*b*-$P4VP_m$ diblock copolymer template[a] - SFM measured dimensions in nm. (Std. Dev.)	
	PS_{1392}-*b*-$P4VP_{471}$	PS_{552}-*b*-$P4VP_{174}$
FWHM[b]	54 (5)	35 (5)
Height	26 (3)	14 (3)
Periodicity	101 (8)	63 (8)

[a] – *n* and *m* represent the average number of repeat units of the PS and P4VP blocks, respectively.
[b] – full width at half maximum.

Table S3. Comparison of twenty compositionally tuned particle clusters synthesized from immersion into 100 mM H_2SO_4 with 10 mM [H_2IrCl_6 + H_2PtCl_6].

Pt : Ir molar ratio in immersion bath	NP and Cluster Parameters	PS_n-*b*-$P4VP_m$ Diblock copolymer template[a] and TEM estimated dimensions (Std. Dev.)	
		PS_{1392}-*b*-$P4VP_{471}$	PS_{552}-*b*-$P4VP_{174}$
10 : 0	NP Diameter[b]	10 ± 4 nm	6 ± 3 nm
	NPs per Cluster[c]	2 ± 1	7 ± 3
	Periodicity[d]	116 ± 7 nm	56 ± 9 nm
	Stoichiometry Estimated by XPS	$Pt_{100}Ir_0$	$Pt_{100}Ir_0$
9.75 : 0.25	NP Diameter[b]	6 ± 2 nm	6 ± 3 nm
	NPs per Cluster[c]	7 ± 4	4 ± 2
	Periodicity[d]	145 ± 14 nm	71 ± 11 nm
	Stoichiometry Estimated by XPS	$Pt_{97}Ir_3$	$Pt_{97}Ir_3$
9.5 : 0.5	NP Diameter[b]	4 ± 1 nm	6 ± 2 nm
	NPs per Cluster[c]	6 ± 3	4 ± 2
	Periodicity[d]	144 ± 19 nm	74 ± 11 nm
	Stoichiometry Estimated by XPS	$Pt_{91}Ir_9$	$Pt_{79}Ir_{21}$
9.0 : 1.0	NP Diameter[b]	12 ± 3 nm	7 ± 2 nm
	NPs per Cluster[c]	2.4 ± 1.2	1.4 ± 0.7
	Periodicity[d]	122 ± 14 nm	54 ± 10 nm
	Stoichiometry Estimated by XPS	$Pt_{60}Ir_{40}$	$Pt_{58}Ir_{42}$
8.0 : 2.0	NP Diameter[b]	13 ± 5	9 ± 1
	NPs per Cluster[c]	1.6 ± 1.0	1.8 ± 1.2
	Periodicity[d]	116 ± 14 nm	45 ± 7 nm
	Stoichiometry Estimated by XPS	$Pt_{33}Ir_{67}$	$Pt_{36}Ir_{64}$
7.5 : 2.5	NP Diameter[b]	11 ± 3	9 ± 1
	NPs per Cluster[c]	1.4 ± 0.9	1.2 ± 0.5
	Periodicity[d]	120 ± 10 nm	45 ± 5 nm
	Stoichiometry Estimated by XPS	$Pt_{36}Ir_{64}$	$Pt_{28}Ir_{72}$
7.0 : 3.0	NP Diameter[b]	9 ± 1	9 ± 1
	NPs per Cluster[c]	2.4 ± 1.1	1.2 ± 0.5
	Periodicity[d]	128 ± 7 nm	49 ± 8 nm
	Stoichiometry Estimated by XPS	$Pt_{18}Ir_{82}$ [δ]	$Pt_{20}Ir_{80}$
5.0 : 5.0	NP Diameter[b]	11 ± 3	10 ± 1
	NPs per Cluster[c]	2.2 ± 1.3	1.2 ± 0.4
	Periodicity[d]	112 ± 15 nm	49 ± 8 nm
	Stoichiometry Estimated by XPS	$Pt_{19}Ir_{81}$	$Pt_{16}Ir_{84}$
2.4 : 7.6	NP Diameter[b]	11 ± 3	8 ± 1
	NPs per Cluster[c]	1.5 ± 0.7	1.2 ± 0.6
	Periodicity[d]	111 ± 18 nm	55 ± 8 nm
	Stoichiometry Estimated by XPS	$Pt_{18}Ir_{82}$ [γ]	$Pt_{11}Ir_{89}$
0 : 10	NP Diameter[b]	13 ± 5 nm	10 ± 4 nm
	NPs per Cluster[c]	n/a[*]	n/a[*]
	Periodicity[d]	123 ± 13 nm	66 ± 12 nm
	Stoichiometry Estimated by XPS	Pt_0Ir_{100}	Pt_0Ir_{100}

[a] *n* and *m* represent the average number of repeat units of the PS and P4VP blocks, respectively. [b] Average of 100 particles. [c] Average of 25 clusters. [d] Average of 15 clusters. [δ] $Pt_{18}Ir_{82}$ estimated stoichiometry from the 7.0:3.0 bath. [γ] $Pt_{18}Ir_{82}$ estimated stoichiometry from the 2.4:7.6 bath. [*] Continuous metal phase present in nanoring formation.

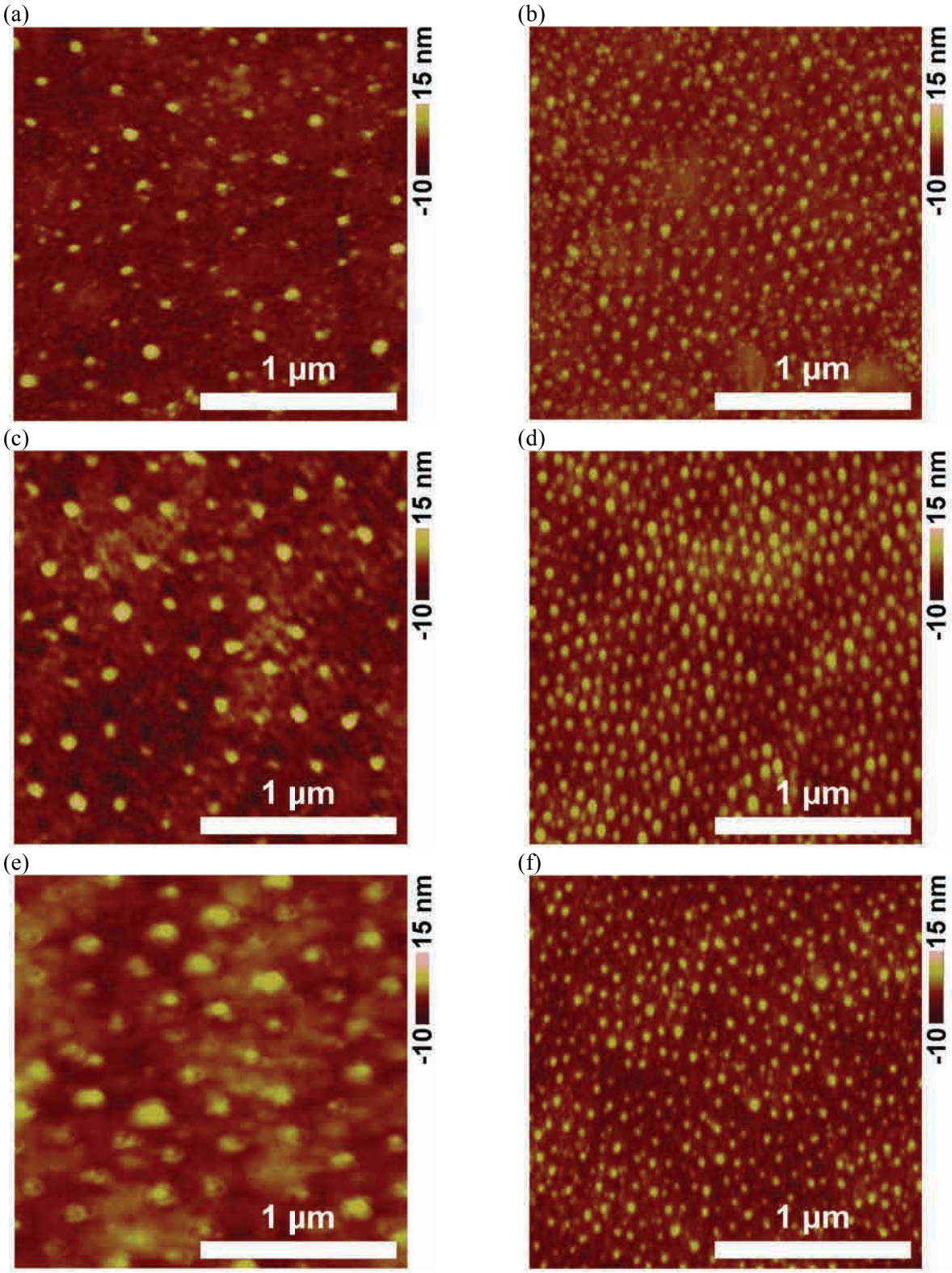

Figure S1. SFM images of arrays of Pt_xIr_{100-x} NP clusters generated from the PS_{1392}-*b*-$P4VP_{471}$ (a, c, e) and the PS_{552}-*b*-$P4VP_{174}$ (b, d, f) templates on ITO electrodes. The composition values of Pt_xIr_{100-x} NPs in these samples were determined by XPS and are: (a) $Pt_{33}Ir_{67}$, (b) $Pt_{36}Ir_{64}$, (c) $Pt_{18}Ir_{82}{}^{\delta}$, (d) $Pt_{20}Ir_{80}$, (e) $Pt_{19}Ir_{81}$, and (f) $Pt_{16}Ir_{84}$.

(a)

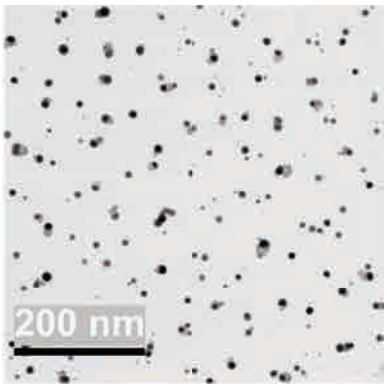

(b)

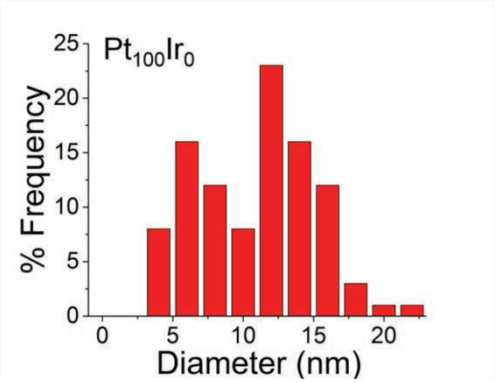

(c)

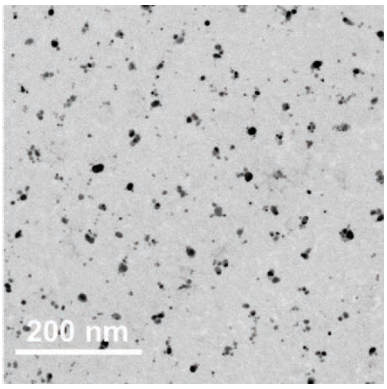

(d)

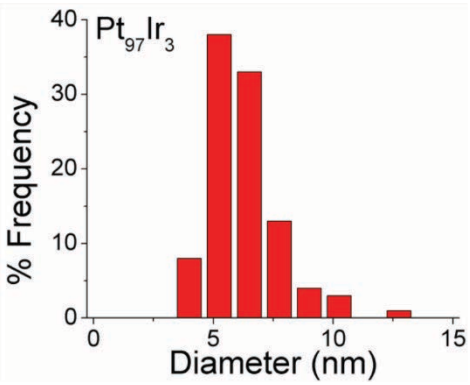

(e)

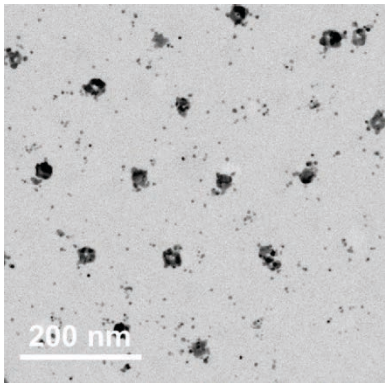

(f)

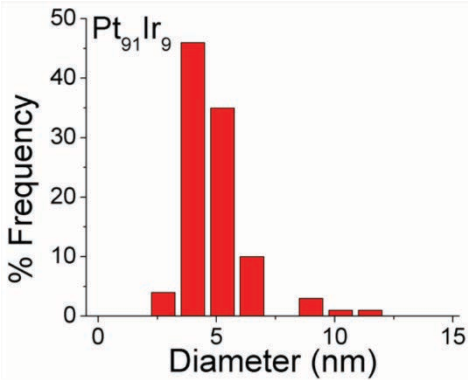

(g)

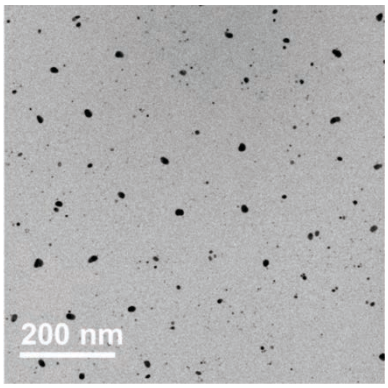

(h)

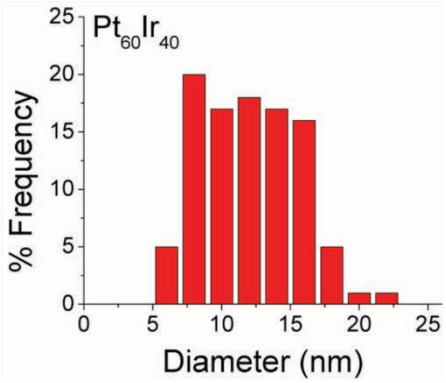

(i)

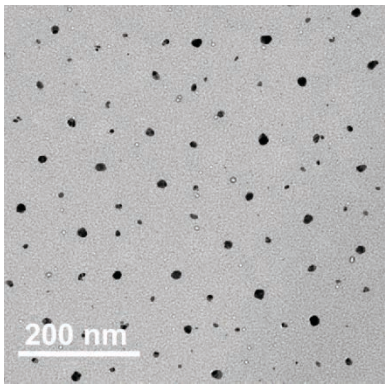

(j)

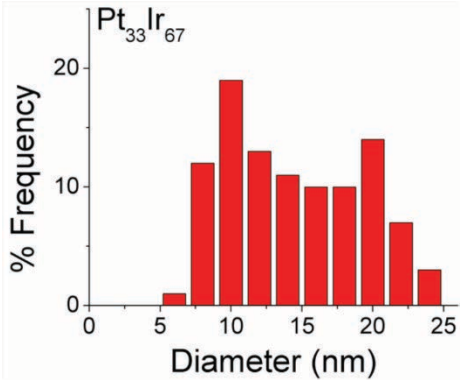

(k)

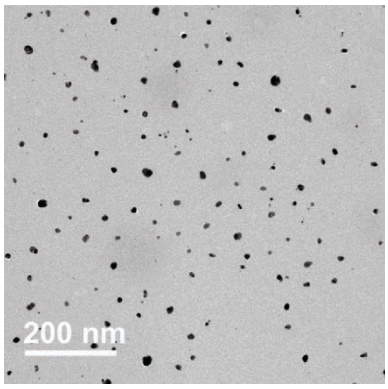

(l)

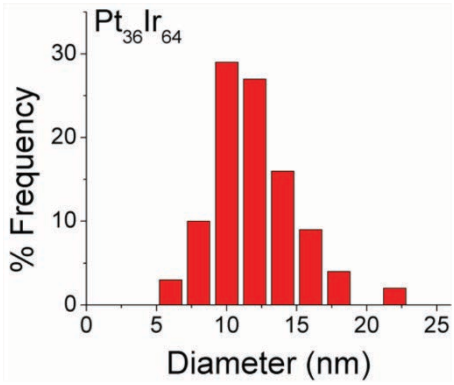

(m)

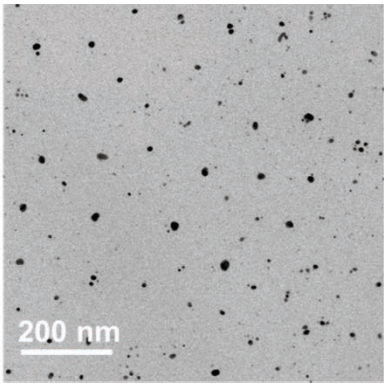
200 nm

(n)

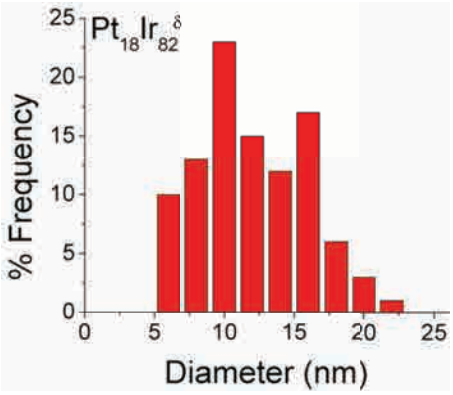
Pt18Ir82δ
% Frequency
Diameter (nm)
0
5
10
15
20
25

(o)

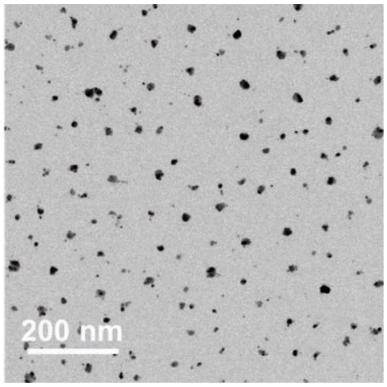
200 nm

(p)

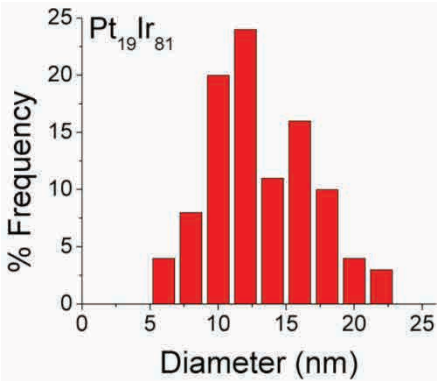
Pt19Ir81
% Frequency
Diameter (nm)
0
5
10
15
20
25

(q)

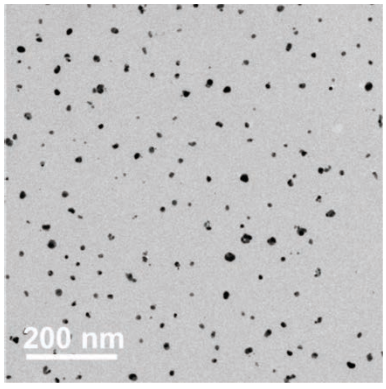
200 nm

(r)

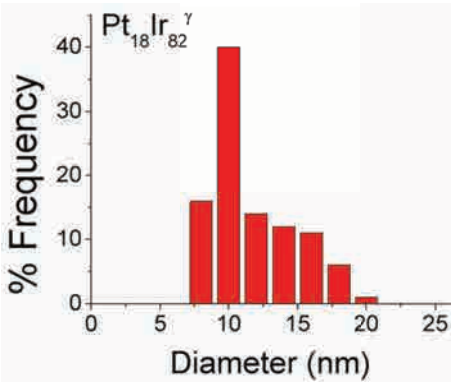
Pt18Ir82γ
% Frequency
Diameter (nm)
0
10
20
30
40
5
15
25

(s) (t)

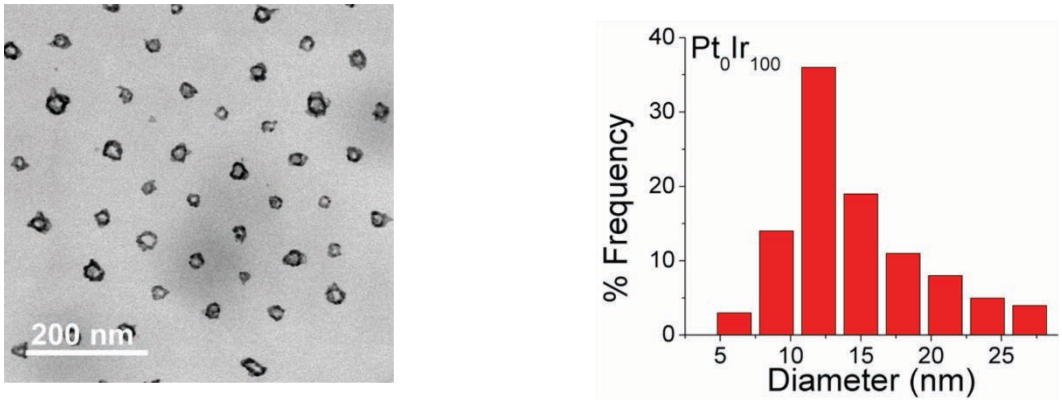

Figure S2. Bright field STEM images (left) and corresponding diameter histograms (right; avg. of 100 particles) of: (a, b) $Pt_{100}Ir_0$, (c, d) $Pt_{97}Ir_3$, (e, f) $Pt_{91}Ir_9$, (g, h) $Pt_{60}Ir_{40}$, (i, j) $Pt_{33}Ir_{67}$, (k, l) $Pt_{36}Ir_{64}$, (m, n) $Pt_{18}Ir_{82}^{\delta}$, (o, p) $Pt_{19}Ir_{81}$, (q, r) $Pt_{18}Ir_{82}^{\gamma}$, and (s, t) Pt_0Ir_{100} synthesized with the PS_{1392}-*b*-$P4VP_{471}$ template.

(a)

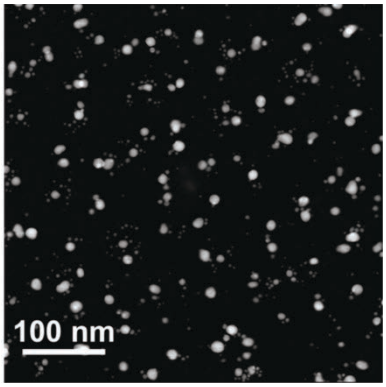

(b)

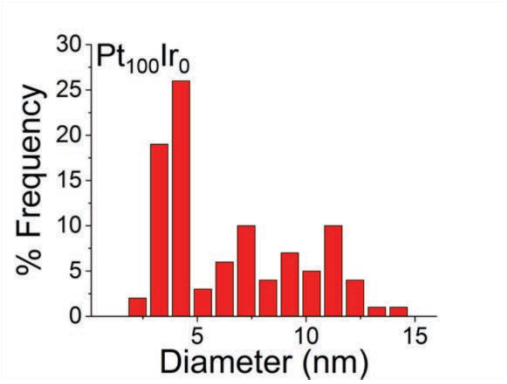

(c)

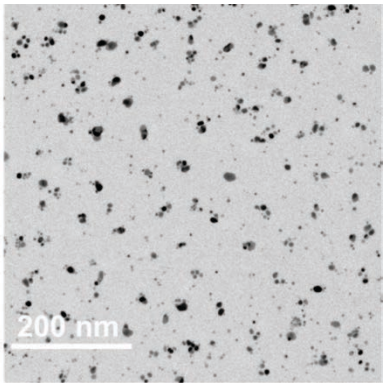

(d)

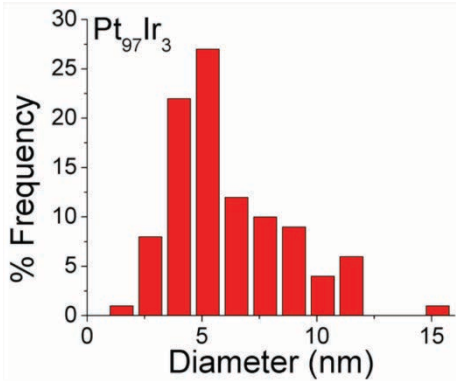

(e)

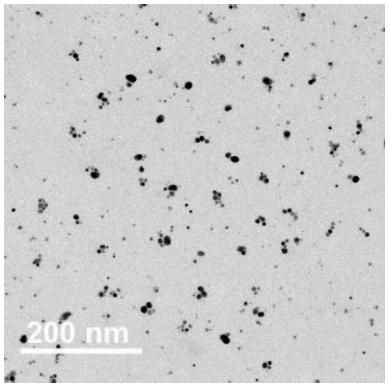

(f)

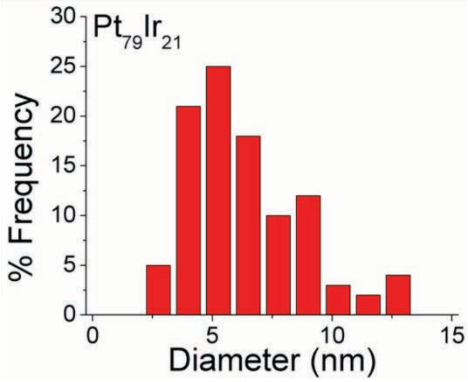

(g)

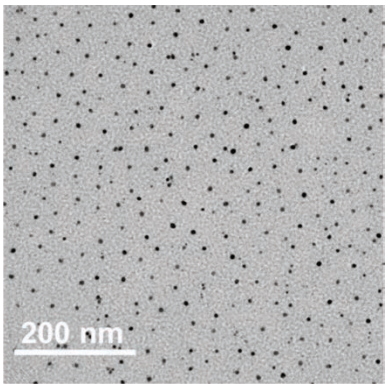

(h)

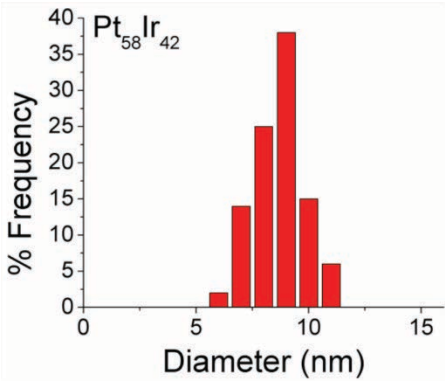

(i)

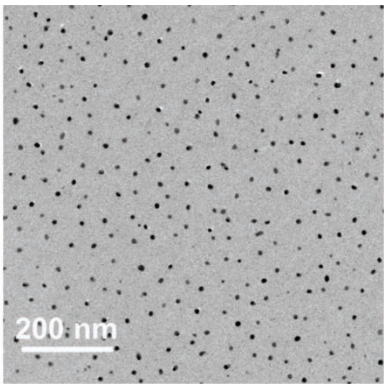

(j)

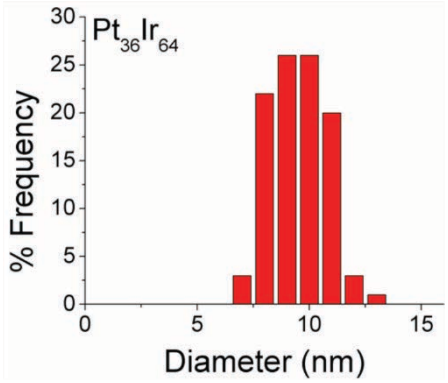

(k)

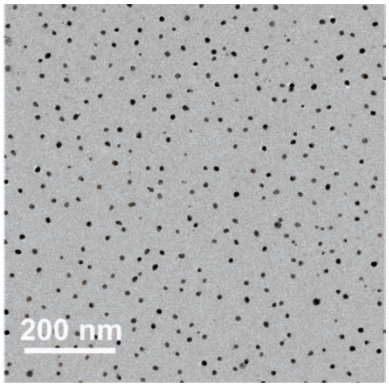

(l)

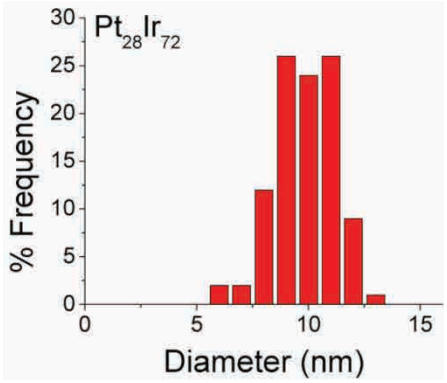

(m)

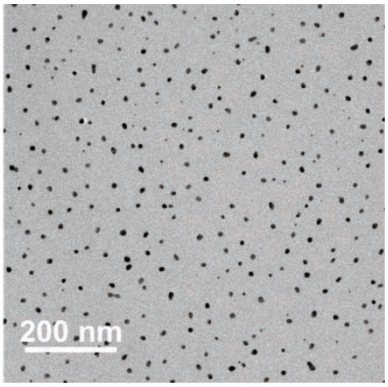

(n)

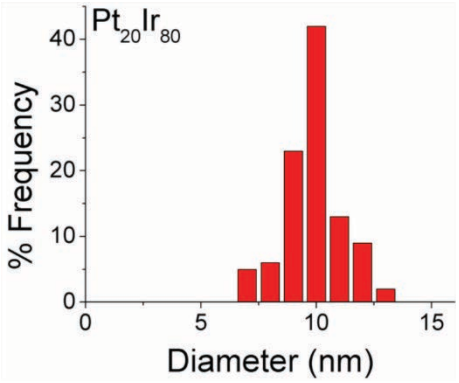

(o)

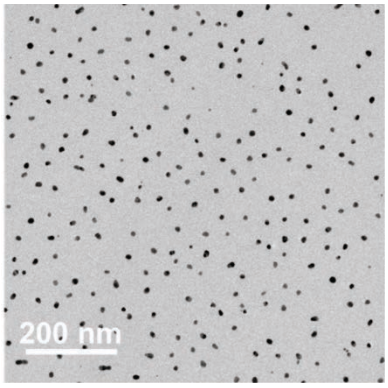

(p)

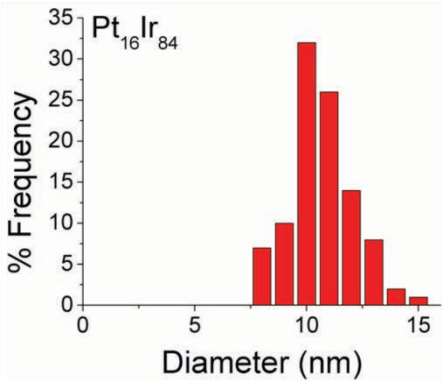

(q)

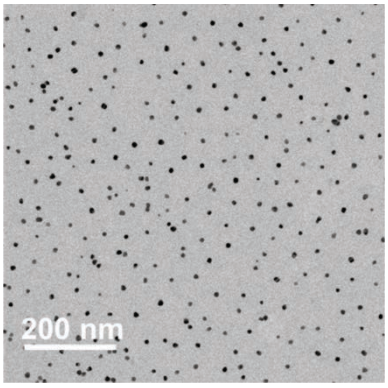

(r)

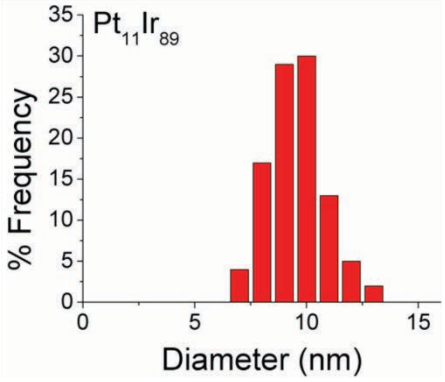

(s) (t)

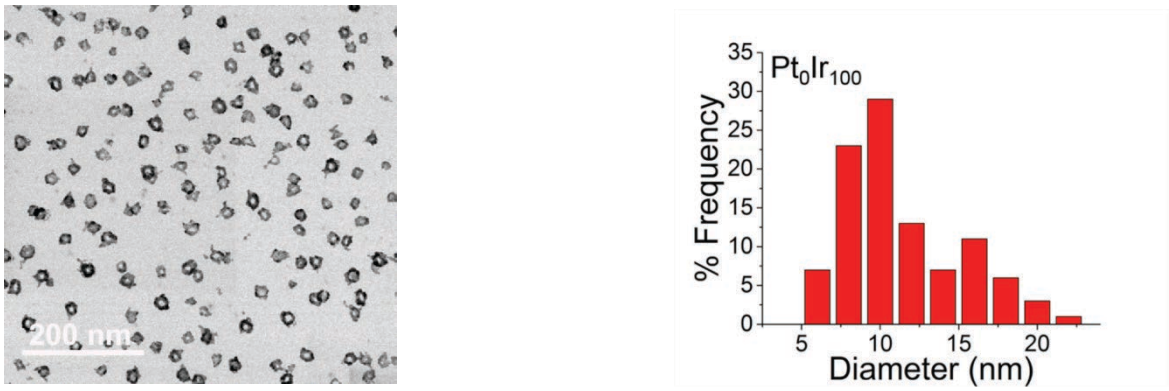

Figure S3. Bright field and HAADF STEM/TEM images (left) and corresponding diameter histograms (right; avg. of 100 particles) of: (a, b) $Pt_{100}Ir_0$, (c, d) $Pt_{97}Ir_3$, (e, f) $Pt_{79}Ir_{21}$, (g, h) $Pt_{58}Ir_{42}$, (i, j) $Pt_{36}Ir_{64}$, (k, l) $Pt_{28}Ir_{72}$, (m, n) $Pt_{20}Ir_{80}$, (o, p) $Pt_{16}Ir_{84}$, (q, r) $Pt_{11}Ir_{89}$, and (s, t) Pt_0Ir_{100} synthesized with the PS_{552}-*b*-$P4VP_{174}$ template.

(a)

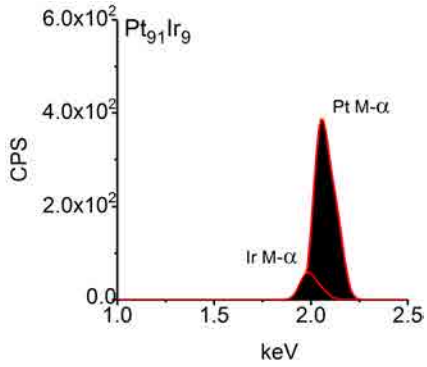
6.0x10²
4.0x10²
2.0x10²
0.0
CPS
Pt91Ir9
Pt M-α
Ir M-α
1.0
1.5
2.0
2.5
keV

(b)

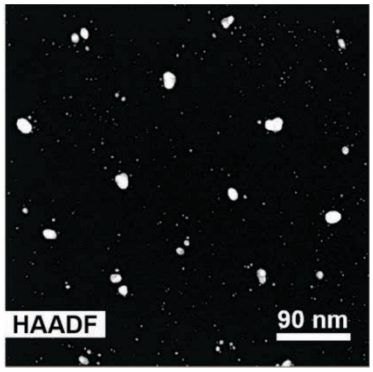
HAADF
90 nm

(c)

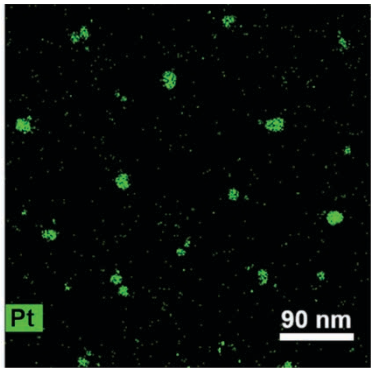
Pt
90 nm

(d)

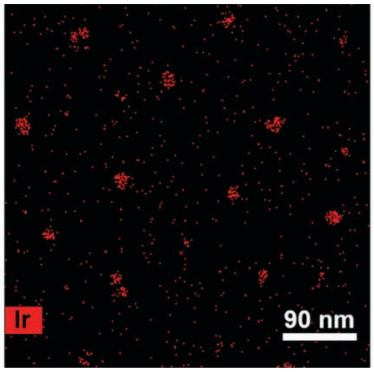
Ir
90 nm

(e)

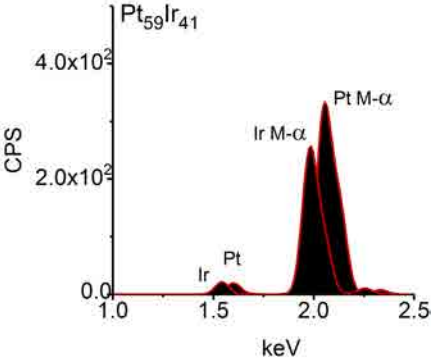
Pt59Ir41
4.0x10²
2.0x10²
0.0
CPS
Pt M-α
Ir M-α
Pt
Ir
1.0
1.5
2.0
2.5
keV

(f)

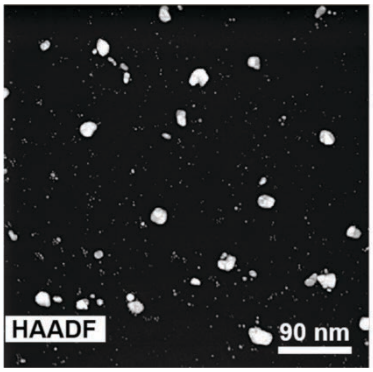
HAADF
90 nm

(g)

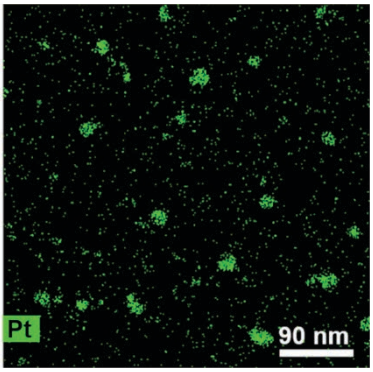
Pt
90 nm

(h)

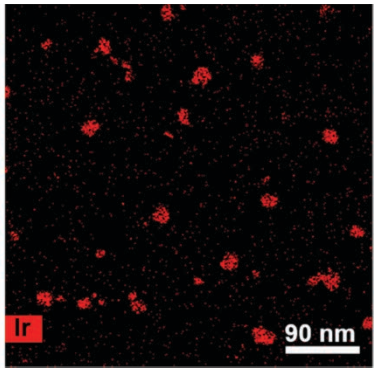
Ir
90 nm

(i)

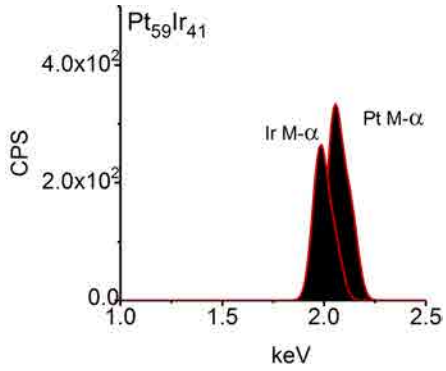

(j)

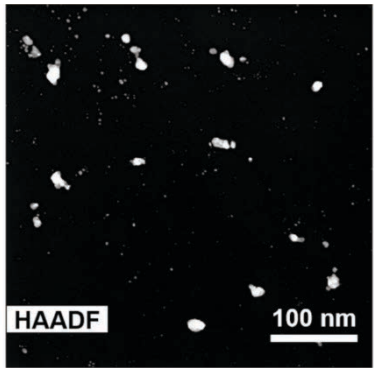

(k)

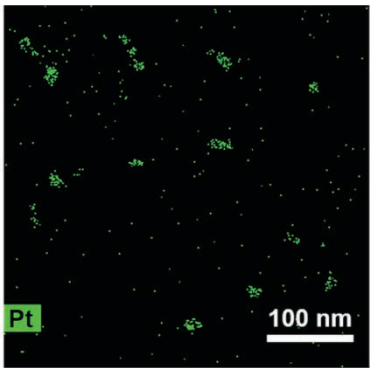

(l)

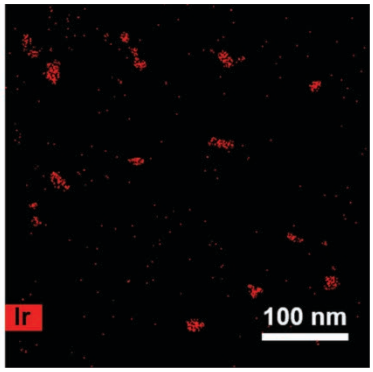

(m)

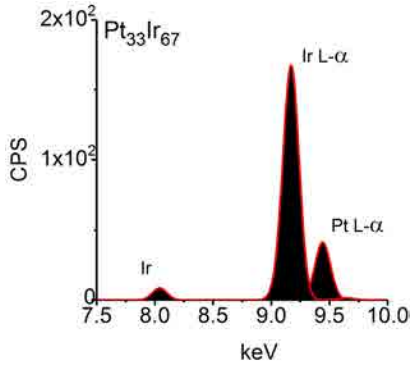

(n)

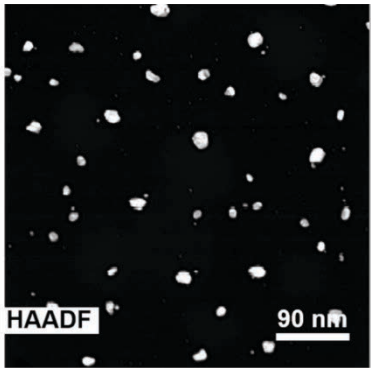

(o)

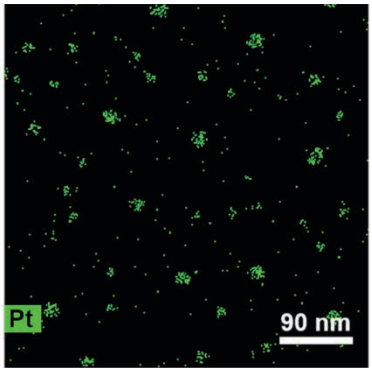

(p)

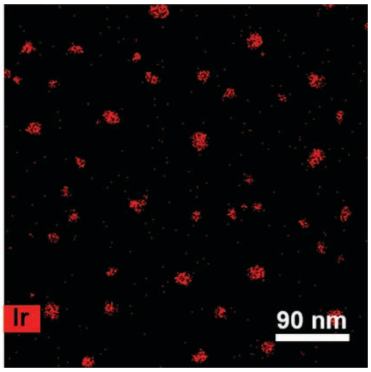

(q)

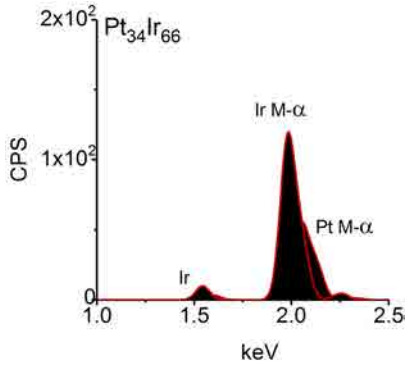

(r)

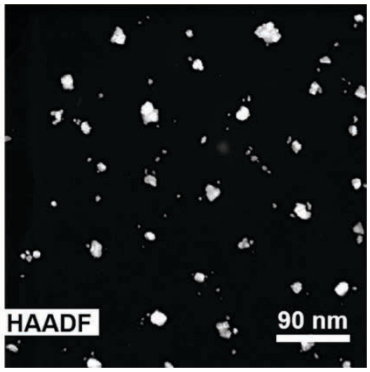

(s)

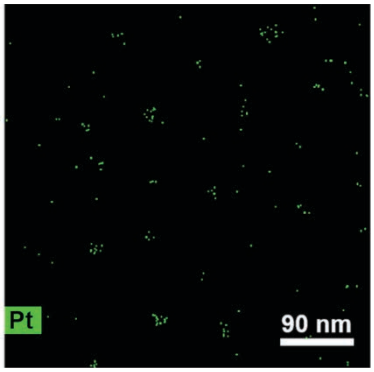

(t)

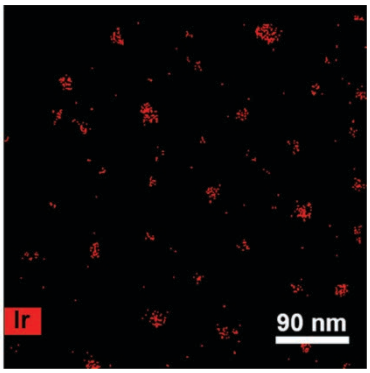

(u)

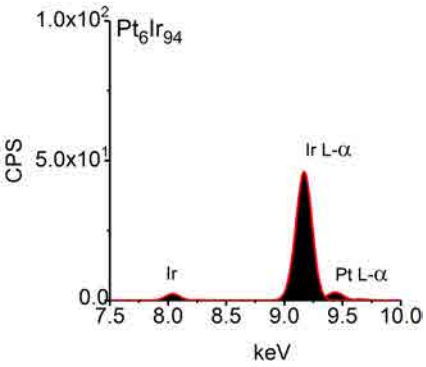

(v)

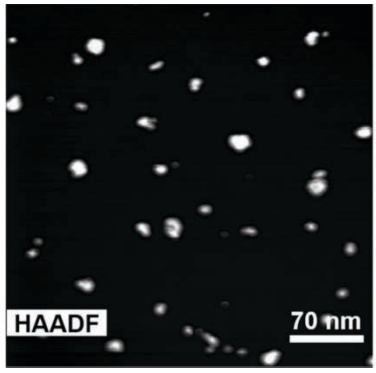

(w)

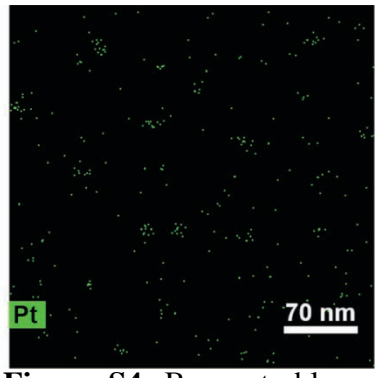

(x)

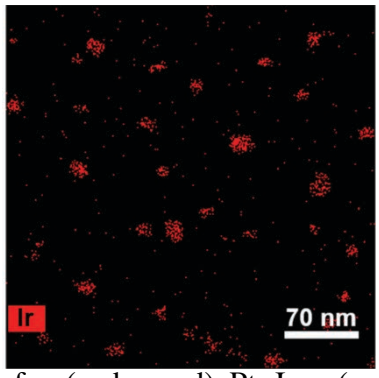

Figure S4. Bremsstrahlung corrected EDS spectra for (a, b, c, d) $Pt_{60}Ir_{40}$, (e, f, g, h) $Pt_{33}Ir_{67}$, (i, j, k, l) $Pt_{36}Ir_{64}$, (m, n, o, p) $Pt_{18}Ir_{82}{}^{\delta}$, (q, r, s, t) $Pt_{19}Ir_{81}$, and (u, v, w, x) $Pt_{18}Ir_{82}{}^{\gamma}$ NPs synthesized with the PS_{1392}-*b*-$P4VP_{471}$ template. The inset labels in each graph refer to the EDS-estimated Pt:Ir ratios for 0.12 μm^2 areas while those in the caption refer to those determined by XPS.

(a)

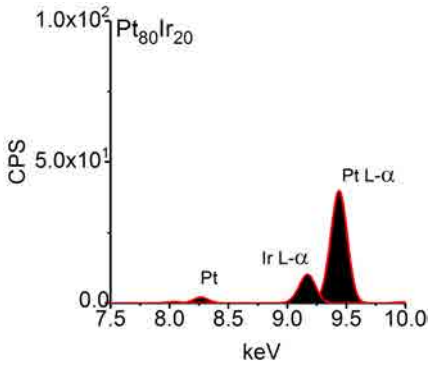
$Pt_{80}Ir_{20}$
1.0x10²
5.0x10¹
0.0
CPS
Pt L-α
Ir L-α
Pt
7.5 8.0 8.5 9.0 9.5 10.0
keV

(b)

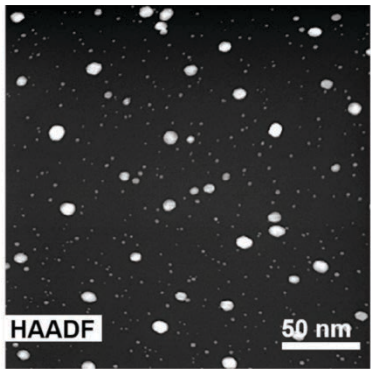
HAADF
50 nm

(c)

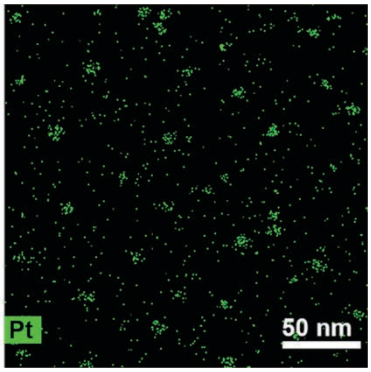
Pt
50 nm

(d)

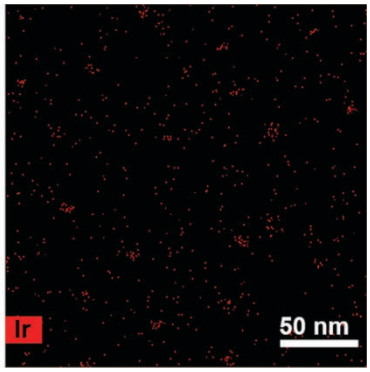
Ir
50 nm

(e)

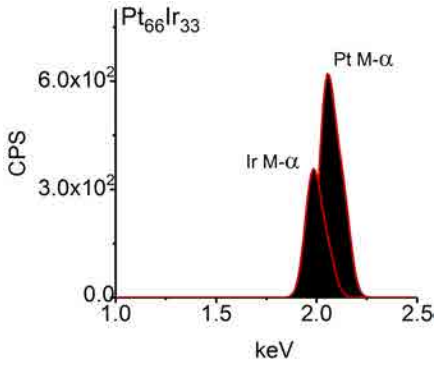
$Pt_{66}Ir_{33}$
6.0x10²
3.0x10²
0.0
CPS
Pt M-α
Ir M-α
1.0 1.5 2.0 2.5
keV

(f)

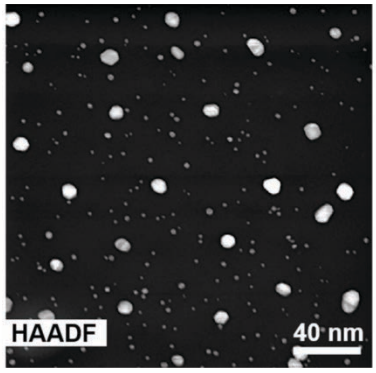
HAADF
40 nm

(g)

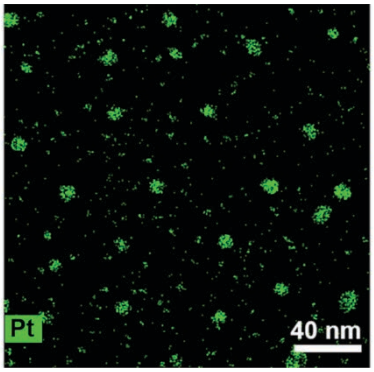
Pt
40 nm

(h)

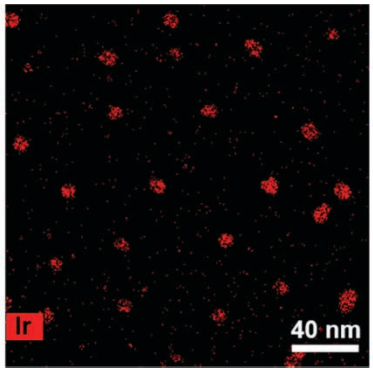
Ir
40 nm

(i)

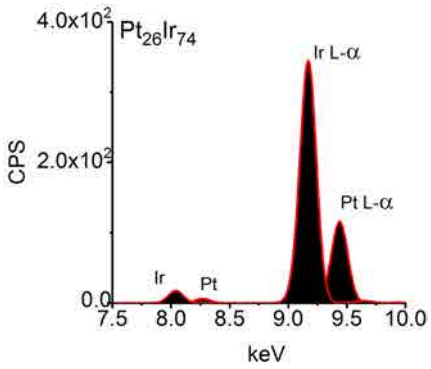

(j)

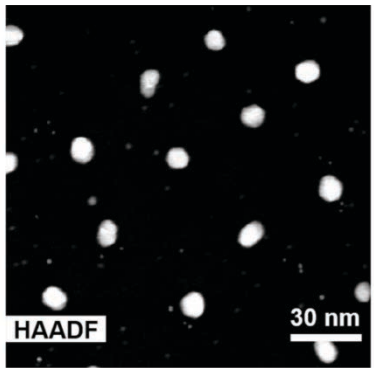

(k)

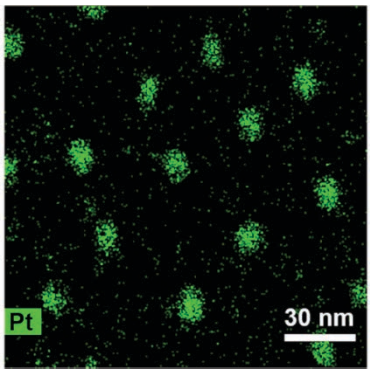

(l)

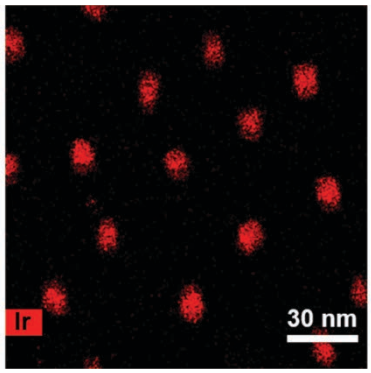

(m)

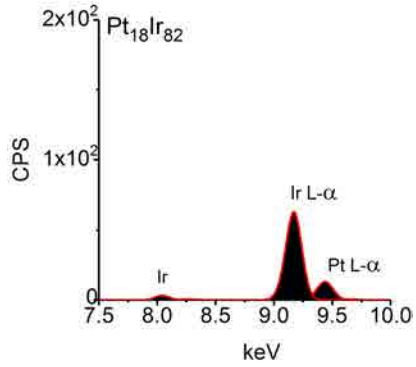

(n)

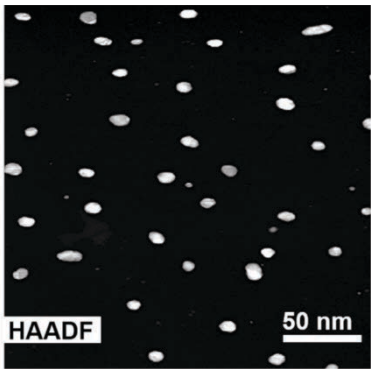

(o)

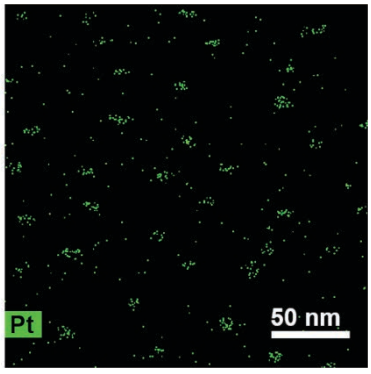

(p)

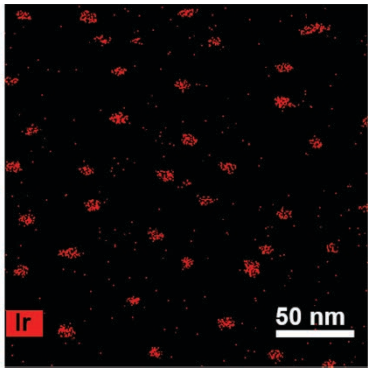

(q)

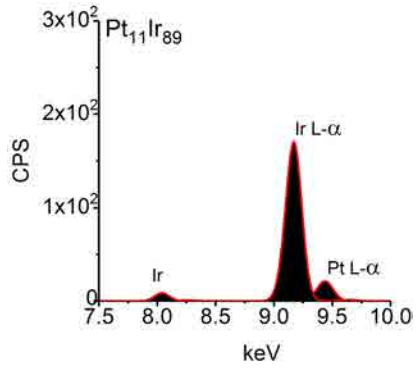

(r)

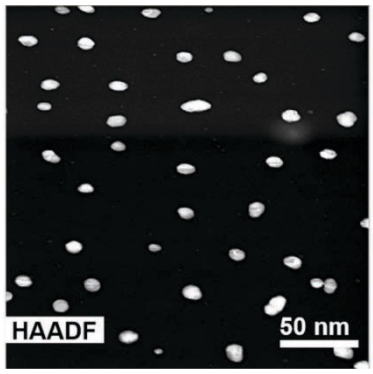

(s)

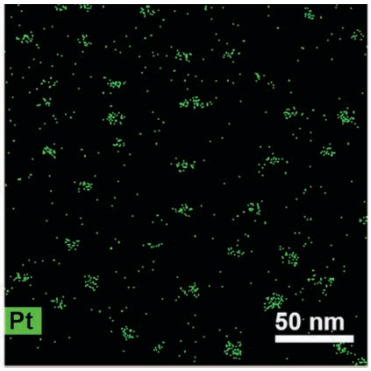

(t)

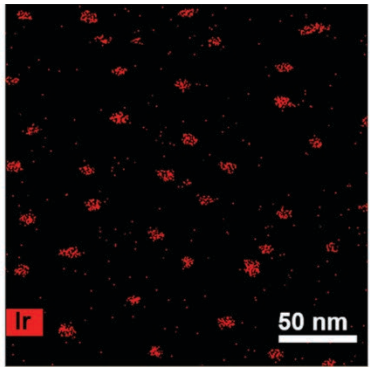

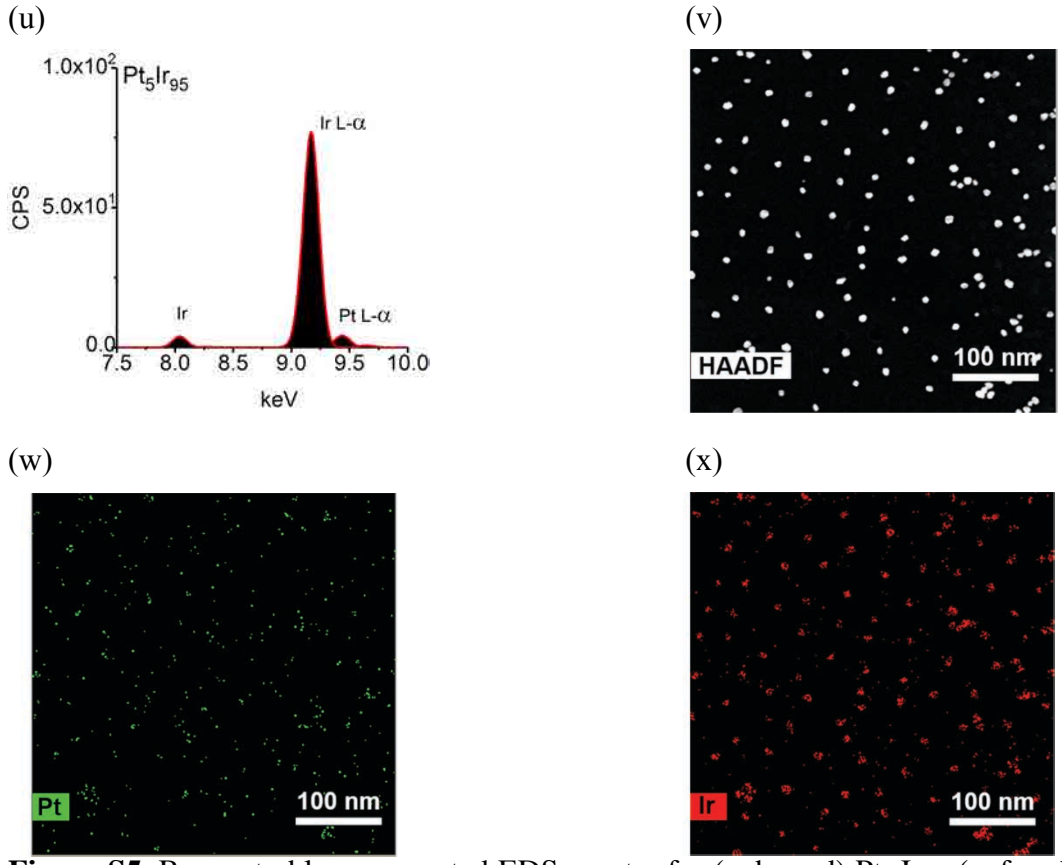

Figure S5. Bremsstrahlung corrected EDS spectra for (a, b, c, d) $Pt_{58}Ir_{42}$, (e, f, g, h) $Pt_{36}Ir_{64}$, (i, j, k, l) $Pt_{28}Ir_{72}$, (m, n, o, p) $Pt_{20}Ir_{80}$, (q, r, s, t) $Pt_{16}Ir_{84}$, and (u, v, w, x) $Pt_{11}Ir_{89}$ NPs synthesized with the PS_{552}-*b*-$P4VP_{174}$ template. The inset labels refer to the EDS-estimated Pt:Ir ratios for 0.056 μm^2 areas while those in the caption refer to those determined by XPS.

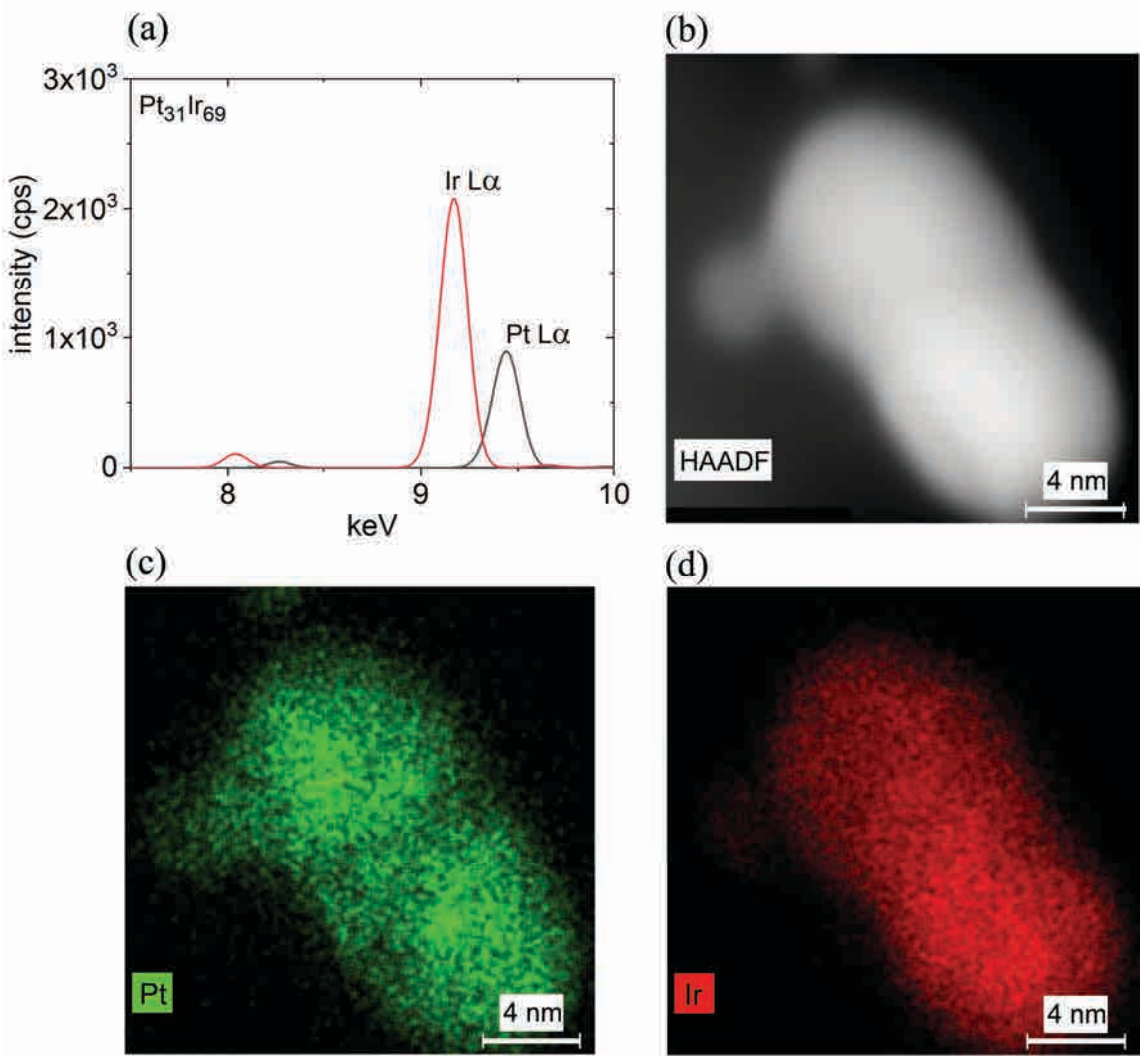

Figure S6. The Bremsstrahlung corrected high-resolution mapping of the EDS spectra for a single NP synthesized with the PS_{552}-*b*-$P4VP_{174}$ template from a loading bath of 8.0:2.0 with an XPS-estimated composition of $Pt_{36}Ir_{64}$. The plot in (a) shows the intensity of the Lα emission obtained from the NP shown in the (b) HAADF image. The (c) Pt elemental map and the (d) Ir elemental map are also shown. The inset in (a) is the EDS-estimated composition of the particle.

Shown in Figure S6 and S7 are the HR-TEM images for individual NPs isolated from arrays of clusters of PtIr NPs created from the PS_{1392}-*b*-$P4VP_{471}$ and PS_{552}-*b*-$P4VP_{174}$ templates, respectively. Each image in S6 and S7 shows a crystalline NP with resolved lattice planes for loading baths of 8.0:2.0, 7.5:2.5, and 2.4:7.6 (a-c), respectively. This observation is more clearly identified by the Fast-Fourier Transform (FFT) of these images, which are presented as insets. These FFT-images reveal pronounced intensities at the reciprocal radii positions labelled by Miller indices in the associated figures. The highlighted intensities in the FFT of the TEM image in Figure S6 a-c correspond to {111}, {111} and {200} lattice planes with unit cell distances of 3.90, 3.85 and 3.81 Å, respectively. Figure S7 a-c show individual particles with FFT insets that correspond to unit cell distances of 3.87, 3.86, and 3.83 Å for lattice planes of {111}. The average lattice constants for Pt and Ir are 3.92 and 3.84 Å, respectively.[S11-S12] The unit cell dimensions are, therefore, in close agreement with bulk solid solutions of Pt and Ir[S13-S16] and further validate alloy structure inferred from STEM-EDS data.

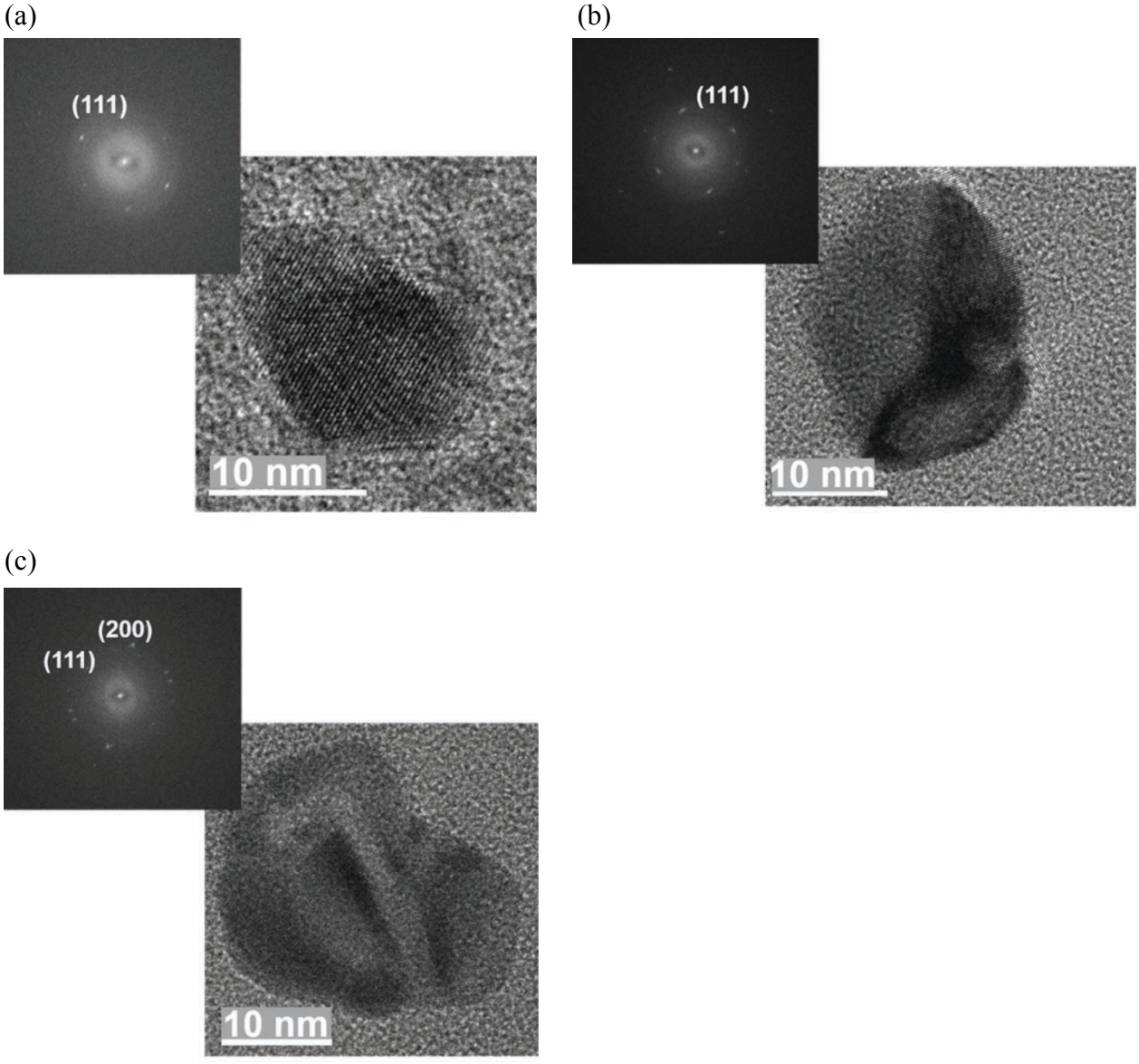

Figure S7. HR-TEM images of single PtIr NPs for (a) $Pt_{33}Ir_{67}$, (b) $Pt_{36}Ir_{64}$, and (c) $Pt_{18}Ir_{82}$[γ] synthesized from the PS_{1392}-*b*-$P4VP_{471}$ template. The insets are the corresponding Fast-Fourier

Transform (FFT) images with the labeled assignments included for the lattice planes observed in the HR-TEM images.

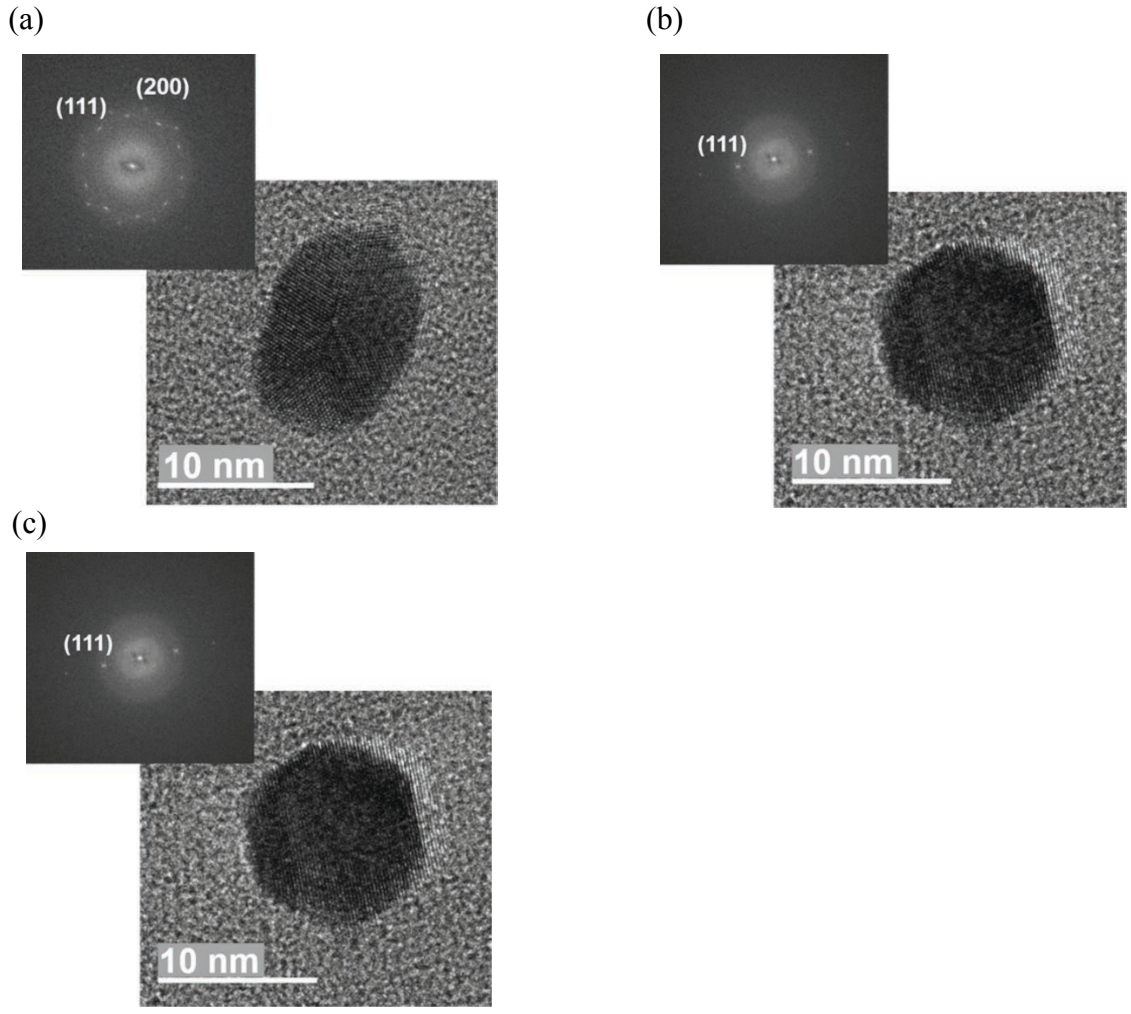

Figure S8. HR-TEM images of single PtIr NPs for (a) $Pt_{36}Ir_{64}$, (b) $Pt_{28}Ir_{72}$, and (c) $Pt_{11}Ir_{89}$, synthesized from the PS_{552}-*b*-$P4VP_{174}$ template. The insets are the corresponding FFT images with the labeled assignments included for the lattice planes observed in the HR-TEM images.

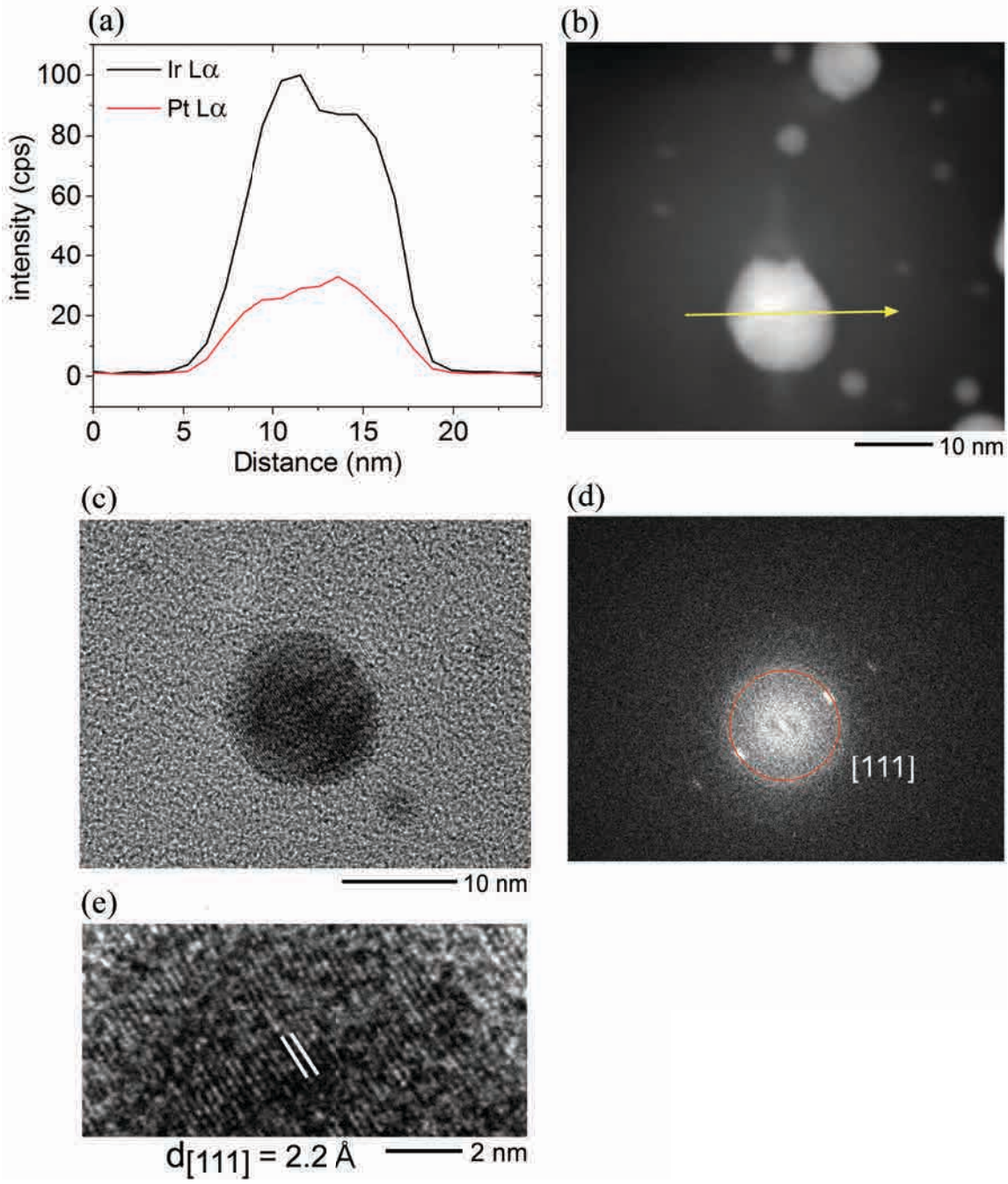

Figure S9. Representative (a) EDS line-scan profile of a single NP synthesized from the PS_{552}-*b*-$P4VP_{174}$ template from a Pt:Ir loading bath of 8.0:2.0. The corresponding (b) HAADF is shown and the yellow line indicates the direction of the line profile. The matching (c) HR-TEM image and (d) FFT image with the labeled assignment indicate a {111} lattice plane. In (e) the lattice fringe pattern suggests a d-spacing of 2.2 Å, which matches the calculated d-spacing from the FFT image in (d). The calculated d-spacing of 2.2 Å is in agreement with the {111} plane d-spacing for a $Pt_{17}Ir_{83}$ composition determined by XRD (JCPDS No. 01-088-1728).

(a) (b)

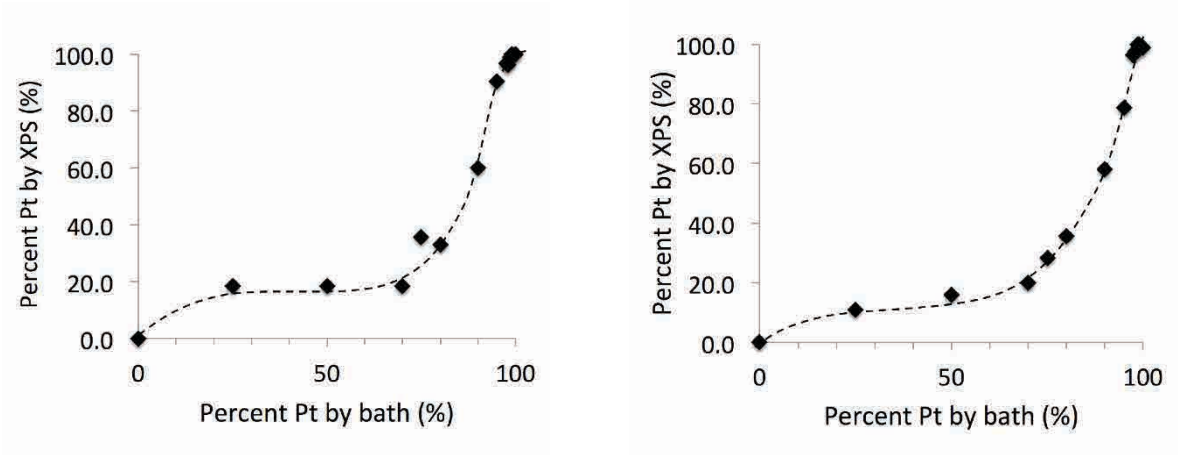

Figure S10. The ICP-MS- and XPS-estimated mass loadings of Pt for the Pt_xIr_{100-x} NPs synthesized from (a) PS_{1392}-*b*-$P4VP_{471}$ and (b) PS_{552}-*b*-$P4VP_{174}$ templates.

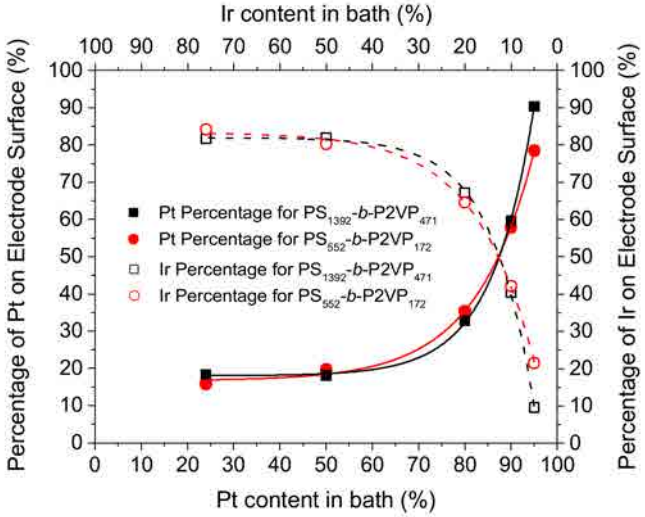

Figure S11. The ICP-MS- and XPS-estimated percentages of Pt (solid symbols) and Ir (open symbols) on the electrode surface for selected bimetallic Pt_xIr_{100-x} NPs synthesized from PS_{1392}-*b*-$P4VP_{471}$ (square symbols) and PS_{552}-*b*-$P4VP_{174}$ (circle symbols) templates.

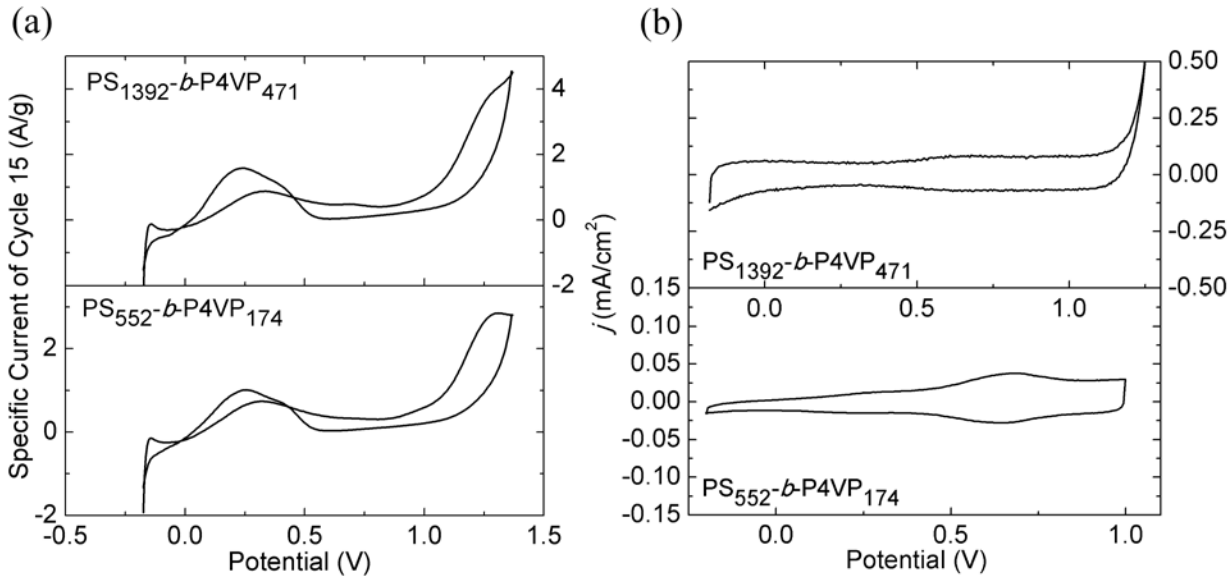

Figure S12. Formic acid oxidation plots for the monometallic NP arrays supported on ITO. The (a) 15th CV cycle of the Pt analogues showing the specific current (normalized for mass loading) and the (b) 2nd CV cycle of the monometallic Ir NP arrays reported in current density, which was determined from the geometric area of the electrode. The CV data was acquired in 100 mM HCOOH and 100 mM H_2SO_4. The notation shown in each of the plots indicates the type of block copolymer used to prepare the NP catalyst arrays. The oxidation of formic acid on Ir NPs does not exhibit any of the characteristics for monometallic Pt or bimetallic Pt_xIr_{100-x} NPs. The cycle 15 I_{1a} and I_3 values for monometallic Pt NPs produced from PS_{1392}-*b*-$P4VP_{471}$ were 2.66 A/g and 4.56 A/g, respectively, while those for the PS_{552}-*b*-$P4VP_{174}$ were 1.14 A/g and 1.60 A/g, respectively.

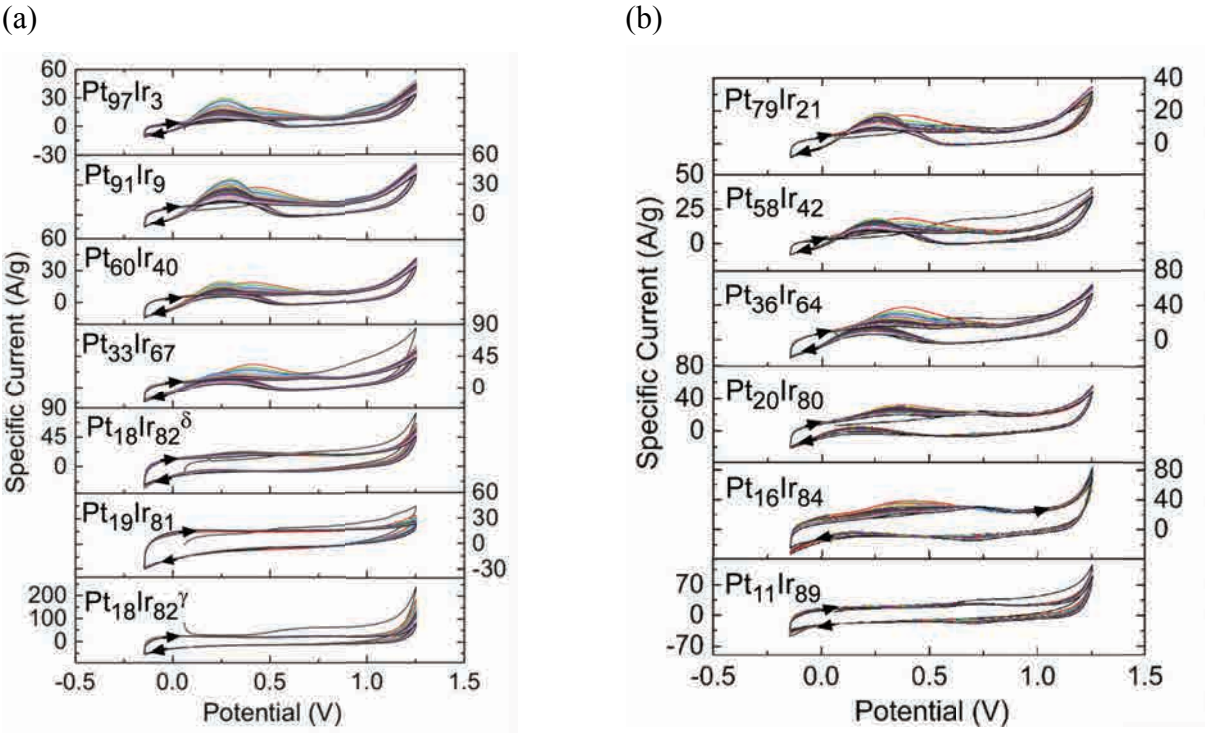

Figure S13. Shown are the 25-cycle CV plots (100 mM H_2SO_4 and 100 mM HCOOH, 10 mV/s) for ITO-supported Pt_xIr_{100-x} NPs synthesized from the (a) PS_{1392}-*b*-$P4VP_{471}$ and (b) PS_{552}-*b*-$P4VP_{174}$ templates. The inset labels refer to the XPS-estimated Pt:Ir ratio of the NP clusters. The arrows indicate the direction of the CV scans.

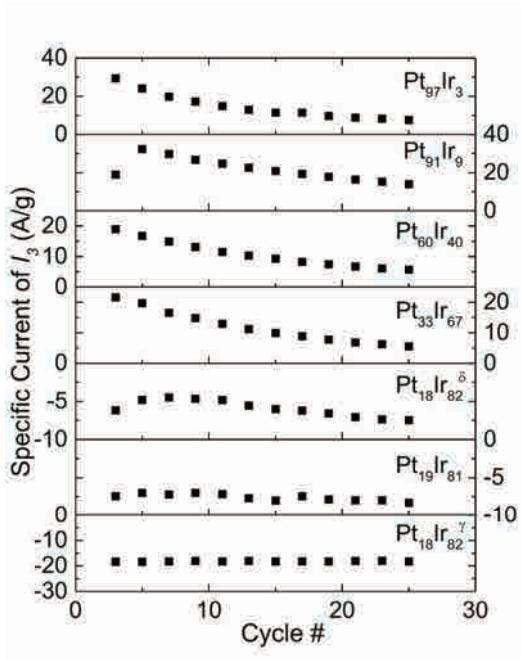

Figure S14. Mass specific current for I_3 versus cycle number for PtIr NP arrays synthesized from PS_{1392}-*b*-$P4VP_{471}$. All PtIr NP arrays are supported on ITO. The CV data was acquired in 100 mM HCOOH and 100 mM H_2SO_4 with a potential scan rate of 10 mV/s. The subscripts in the inset Pt_xIr_{100-x} labels denote the XPS-estimated compositions.

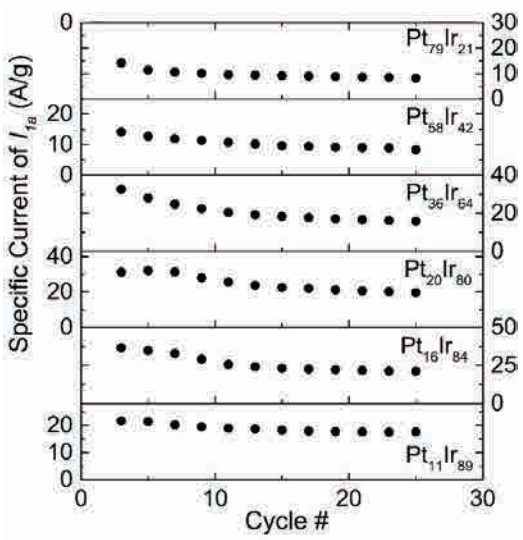

Figure S15. Mass specific current for I_3 versus cycle number for PtIr NP arrays synthesized from PS_{552}-*b*-$P4VP_{174}$. All PtIr NP arrays are supported on ITO. The CV data was acquired in 100 mM HCOOH and 100 mM H_2SO_4 with a potential scan rate of 10 mV/s. The subscripts in the inset Pt_xIr_{100-x} labels denote the XPS-estimated composition.

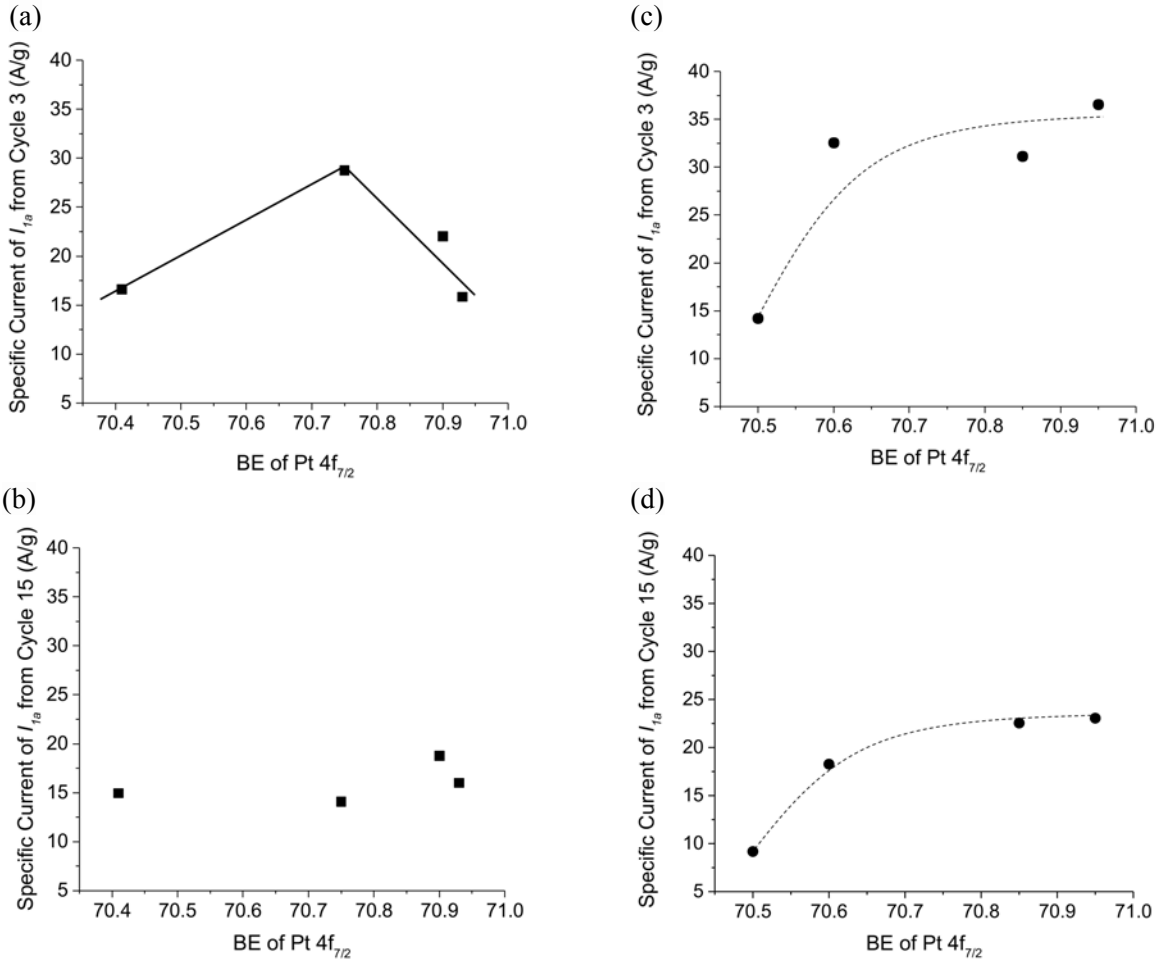

Figure S16. Plot for I_{1a} peak current of Pt_xIr_{100-x} NPs synthesized from PS_{1392}-*b*-$P4VP_{471}$ (square symbols) and PS_{552}-*b*-$P4VP_{174}$ (circle symbols) versus the binding energy for the respective Pt $4f_{7/2}$ peak found by XPS. Data in (a) and (c) were obtained from cycle 3 of a 25 cycle study while data in (b) and (d) were obtained from cycle 15 of a 25 cycle study.

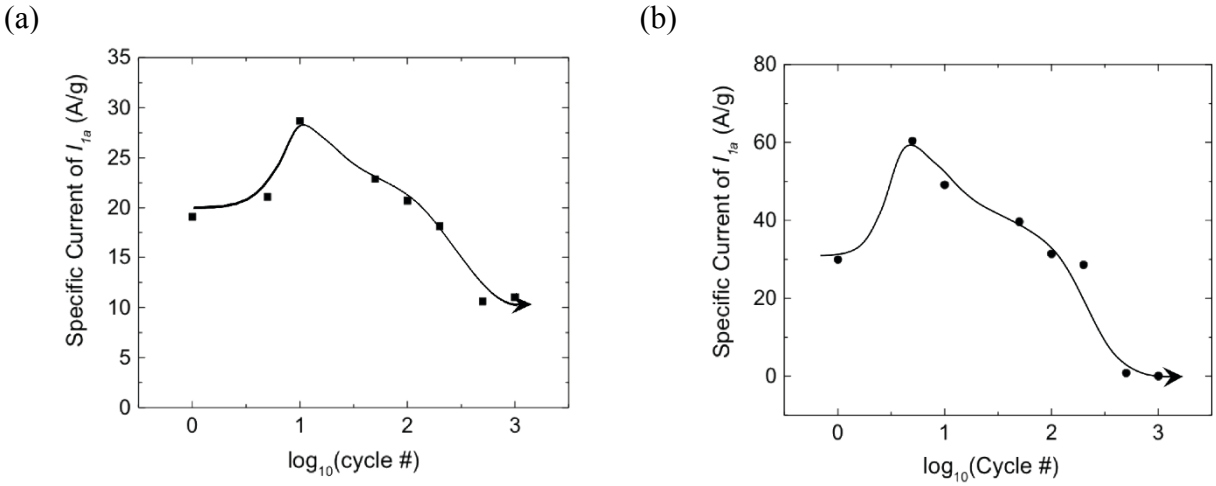

Figure S17. Mass specific current for the formic acid oxidation reaction versus log of cycle number for a multi-cycle study for (a) $Pt_{18}Ir_{82}$ $^{\delta}$ NPs synthesized from PS_{1392}-*b*-$P4VP_{471}$ and (b) $Pt_{20}Ir_{80}$ NPs synthesized from PS_{552}-*b*-$P4VP_{174}$ templates. The trend lines are intended to guide the eye.

References:

(S1) C. Xu; Q. Hao; H. Duan, *J. Mater. Chem A* 2014, **2** (23), 8875-8880.
(S2) S. Hu; L. Scudiero; S. Ha, *Electrochem. Commun.* 2017, **38**, 107-109.
(S3) M. Scofield; C. Koenigsmann; L. Wang; H. Liu; S. S. Wong, *Energy Environ. Sci.* 2015, **8** (1), 350-363.
(S4) S. Hu; F. Munoz; J. Noborikawa; J. Haan; L. Scudiero; S. Ha, *Appl. Catal. B.* 2016, **180**, 758-765.
(S5) W. Chen; J. Kim; S. Sun; S. Chen, *Langmuir* 2007, ***23*** (22), 11303-11310.
(S6) O. Winjobi; Z. Zhang; C. Liang; W. Li, *Electrochim. Acta* 2010, ***55*** (13), 4217-4221.
(S7) R. Wang; C. Wang; W. B. Cai; Y. Ding, *Adv. Mater.* 2010, ***22*** (16), 1845-1848.
(S8) J. Shim; J. Lee; Y. Ye; J. Hwang; S. K. Kim; T. H. Lim; U. Wiesner; J. Lee, *ACS Nano* 2012, ***6*** (8), 6870-6881.
(S9) W. Chen; J. Kim; L. P. Xu; S. Sun; S. Chen, *J. Phys. Chem. C* 2007, ***111*** (36), 13452-13459.
(S10) Y. Z. Lu; W. Chen, *Chem. Commun.* 2011, ***47*** (9) 2541-2543.
(S11) J. B. Xu; T. S. Zhao; W. W. Yang; S. Y. Shen, *Int. J. Hydrogen Energy.* 2010, ***35*** (16), 8699-8706.
(S12) J. Y. Chen; T. Herricks; M. Geissler; Y. N. Xia, *J. Am. Chem. Soc.* 2004, ***126*** (35), 10854-10855.
(S13) E. Irissou; F. Laplante; S. Garbarino; M. Chaker; D. Guay, *J. Phys. Chem. C* 2010, ***114*** (5), 2192-2199.
(S14) H. Okamoto; T. B. Massalski, *J. Phase Equilib.* 1985, ***6*** (1), 46-56.
(S15) A. Suzuki; M. Harada; Y. N. Wu; H. Murakami, *Mater. Trans.* 2005, ***46*** (8), 1760-1763.
(S16) R. E. Bedford; G. Bonnier; H. Mass; F. Pavese, *Metrologia* 1996, ***33*** (2), 133.

Journal of Materials Chemistry A

ARTICLE